Journal of Materials Chemistry C

ROYAL SOCIETY OF CHEMISTRY

PAPER

View Article Online
View Journal | View Issue

Cite this: J. Mater. Chem. C, 2021, 9, 10013

Performance enhancement of a p-Si/n-$ZnGa_2O_4$ heterojunction solar-blind UV photodetector through interface engineering†

Dongyang Han,[ab] Kewei Liu,*[ab] Jialin Yang,[a] Xing Chen,[ab] Binghui Li,[a] Lei Liu[ab] and Dezhen Shen*[ab]

Received 13th April 2021,
Accepted 8th July 2021

DOI: 10.1039/d1tc01705e

rsc.li/materials-c

Interface engineering is an effective way to improve the performance of heterojunction photodetectors (PDs). We have constructed p-Si/n-$ZnGa_2O_4$ heterojunction solar-blind ultraviolet (UV) PDs with and without an SiO_2 interfacial layer and studied the effect of the SiO_2 interfacial layer on device performance in detail. At −1 V bias, the dark current of the device from 3.8×10^{-8} A to 5.7×10^{-12} A was greatly reduced, specifically 6.7×10^3 fold, attributed to the high barrier induced by the insertion of the SiO_2 interfacial layer. With the introduction of the SiO_2 interfacial layer, the photo-to-dark current ratio and the detectivity of the device were greatly improved due to the substantial reduction of dark current. Owing to the insertion of the SiO_2 layer reducing the carrier trapping at the interface defects, the rise and decay times of the device were significantly reduced from 0.96 s/0.88 s to 0.12 s/0.08 s, *i.e.* 8 fold and 11 fold, respectively. Moreover, the large conduction band offset of Si/SiO_2 could effectively block visible-light-generated electrons in Si, thereby suppressing the visible-light response and enhancing the UV-visible rejection ratio of the Si/SiO_2/$ZnGa_2O_4$ PD. Our work has provided a feasible approach for enhancing the performance of Si/wide-bandgap semiconductor heterojunction solar-blind UV PDs.

Introduction

Recently, wide-bandgap $ZnGa_2O_4$ has attracted much attention due to its ideal bandgap (E_g = 4.4–5.2 eV), high carrier mobility (~100 cm^2 V^{-1} s^{-1} at a high free-electron concentration of ~10^{19} cm^{-3}), and excellent structural and thermal stability levels, which make it a new promising candidate for the fabrication of high-performance solar-blind ultraviolet (UV) photodetectors (PDs).[1–4] The semiconductor p–n junction is one of the most common structures of photodetectors, since the built-in electric field of the p–n junction helps separate electrons and holes from photogenerated electron–hole pairs.[5–7] According to the previous reports, $ZnGa_2O_4$ is a naturally n-type ternary oxide semiconductor due to the presence of intrinsic defects such as oxygen vacancies and Ga_{Zn} (with the Zn site occupied by Ga) antisite defects.[8–10] Like other wide-bandgap oxide semiconductors such as ZnO and Ga_2O_3, the p-type doping of $ZnGa_2O_4$ also faces great challenges.[11,12] Therefore, the reported $ZnGa_2O_4$ p–n junction detectors can only be constructed from p–n heterojunctions.[13] In particular, the devices based on p-Si/n-$ZnGa_2O_4$ have shown greater competitiveness and practicality because of their potential development prospects in the field of integrated optoelectronics. However, there are many surface/interface states at the Si/$ZnGa_2O_4$ heterojunction due to the large lattice mismatch between Si and $ZnGa_2O_4$, a feature that slows down the response speed of the device and increases the dark current.[14–16] Moreover, since the bandgap of silicon is 1.12 eV, its absorption and response to visible light reduces the UV-visible rejection ratio of the corresponding UV detectors.[17–19]

Interface engineering, which can be deployed to modify heterojunction interfaces and regulate carrier transport processes, is one of the available effective ways to improve the performances of heterojunction PDs.[20–22] To overcome the above-mentioned issues, the SiO_2 interfacial layer is inserted between the p-Si substrate and the n-$ZnGa_2O_4$ layer. First, the insertion of the SiO_2 layer could modify the interface defect states, and thus improve the response speed of the device.[23–25] Meanwhile, the visible-light-photogenerated electrons from Si would be blocked by the SiO_2 layer due to the large conduction band difference of Si/SiO_2 (ΔE_c = 3.15 eV), thereby suppressing

[a] State Key Laboratory of Luminescence and Applications, Changchun Institute of Optics, Fine Mechanics and Physics, Chinese Academy of Sciences, Changchun 130033, P. R. China. E-mail: liukw@ciomp.ac.cn, shendz@ciomp.ac.cn

[b] Center of Materials Science and Optoelectronics Engineering, University of Chinese Academy of Sciences, Beijing 100049, P. R. China

† Electronic supplementary information (ESI) available. See DOI: 10.1039/d1tc01705e

the visible-light response of the device.[26,27] In this work, p-Si/n-$ZnGa_2O_4$ heterojunction PDs with and without an SiO_2 interfacial layer have been demonstrated, and the influence of the SiO_2 insertion layer on the device performance was systematically studied. With the introduction of the SiO_2 interfacial layer, the dark current of the device was effectively suppressed, and the photo-to-dark current ratio, response speed, UV-visible rejection ratio, and detectivity of the device were greatly enhanced. Moreover, the mechanism of device performance changes was also analyzed in detail. Our work has provided a feasible approach for enhancing the performances of Si/wide-bandgap semiconductor heterojunction solar-blind UV PDs.

Experimental

A single-surface polished 500 μm thick p-Si(100) substrate with a resistivity of ~0.004 Ω cm was cleaned sequentially with trichloroethylene, acetone, alcohol, and deionized water. The SiO_2 layer was obtained by carrying out a rapid thermal oxidation (RTO) of Si at 1000 °C in high-purity oxygen (99.9996%). The $ZnGa_2O_4$ films were grown on both Si and Si/SiO_2 by performing metal–organic chemical vapor deposition (MOCVD). The zinc, gallium and oxygen precursors in the growth process were diethylzinc (99.9999%), trimethylgallium (99.9999%) and high-purity oxygen (99.999%), respectively, and their corresponding flow rates were 20, 40 and 300 sccm, respectively. In addition, the substrate temperature and chamber pressure used for growing the material were 600 °C and 23 torr, respectively. After the growth of the $ZnGa_2O_4$ film, the PDs were made by performing photolithography and sputtering an Au electrode on the surface of the $ZnGa_2O_4$ film and pasting an In electrode on the back surface of the Si substrate as quasi–ohmic contacts (see Fig. S1, ESI† for metal–semiconductor contact properties). The shape of the top Au electrode is shown in Fig. S2 (ESI†). The structures of the Si/$ZnGa_2O_4$ PD and Si/SiO_2/$ZnGa_2O_4$ PD are illustrated in Fig. 1(a).

The crystal structure properties of the $ZnGa_2O_4$ films were evaluated using a Bruker D8GADDS X-ray diffractometer (XRD). The surface and cross-sectional morphologies of the $ZnGa_2O_4$ films were characterized using a HITACHI S-4800 scanning electron microscope (SEM). The current–voltage (*I*–*V*) characteristics and time dependence of the photocurrent (*I*–*t*) of the Si/$ZnGa_2O_4$ PD and those for Si/SiO_2/$ZnGa_2O_4$ PD were measured using an Agilent B1500A semiconductor device analyzer. A 200 W UV-enhanced Xe lamp equipped with a monochromator was used to measure the spectral responses of the devices.

Results and discussion

Fig. 1(b) presents the XRD patterns of $ZnGa_2O_4$ films grown on Si and Si/SiO_2 (see Fig. S3, ESI† for the XRD patterns acquired of

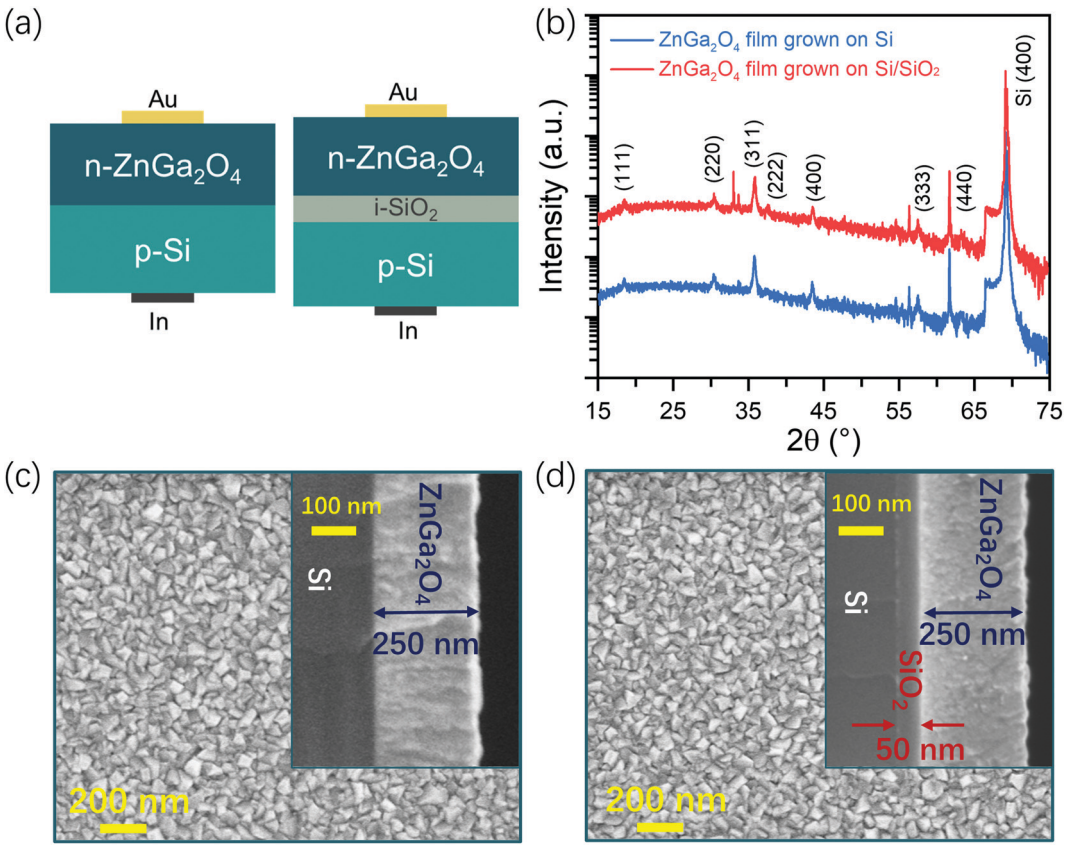

Fig. 1 (a) Schematic illustration of the produced Si/$ZnGa_2O_4$ PD and Si/SiO_2/$ZnGa_2O_4$ PD. (b) XRD patterns of $ZnGa_2O_4$ films grown on Si and Si/SiO_2. (c and d) SEM images of surface and cross-sectional morphologies of the $ZnGa_2O_4$ films grown on (c) Si and (d) Si/SiO_2.

the Si substrate). The $ZnGa_2O_4$ films grown on Si and Si/SiO_2 yielded similar XRD patterns, with diffraction peaks observed at 18.50°, 30.40°, 35.78°, 37.56°, 43.48°, 57.48° and 63.24° and attributed to diffraction from, respectively, the (111), (220), (311), (222), (400), (333) and (440) crystal facets of $ZnGa_2O_4$ (JCPDS No. 38-1240). No SiO_2 peaks in the XRD pattern of $ZnGa_2O_4$ film grown on Si/SiO_2 were observed, indicating an amorphous nature of SiO_2. Fig. 1(c) and (d) show the SEM images acquired of the surface and cross-sectional morphologies of the $ZnGa_2O_4$ films grown on Si and Si/SiO_2, respectively. The surface of the $ZnGa_2O_4$ film on Si and that on Si/SiO_2 were relatively rough with many particles. The cross-sectional SEM images suggested the same thickness of ~250 nm for both $ZnGa_2O_4$ films, and a thickness of ~50 nm for the SiO_2 insulating layer.

Fig. 2(a) and (b) show the *I–V* characteristics of the $Si/ZnGa_2O_4$ PD and $Si/SiO_2/ZnGa_2O_4$ PD in the dark and under 254 nm wavelength UV light illumination with an intensity of 1020 μW cm^{-2}, respectively. As seen in Fig. 2(a) and Fig. S4 (ESI†), both devices exhibited obvious rectifying behaviors in the dark. With the introduction of the SiO_2 interfacial layer, the rectification ratio of the devices at ±5 V greatly increased, specifically from 1.3×10^2 to 2.1×10^6, due to a significant suppression of the reverse dark current. The decrease in reverse dark current of the $Si/SiO_2/ZnGa_2O_4$ PD can be mainly attributed to the high barrier induced by the insertion of the SiO_2 interfacial layer. At −1 V bias, the dark current of the device significantly decreased, specifically 6.7×10^3 fold, from 3.8×10^{-8} A to 5.7×10^{-12} A upon including the SiO_2 layer. Under the 254 nm wavelength UV light illumination, the $Si/ZnGa_2O_4$ PD exhibited a higher photocurrent than did the $Si/SiO_2/ZnGa_2O_4$ PD. The photo-to-dark current ratio (PDCR) is one of the important parameters for evaluating the performance of a PD and can be expressed using the equation[7]

$$\mathrm{PDCR} = (I_{\mathrm{photo}} - I_{\mathrm{dark}})/I_{\mathrm{dark}},$$

where I_{photo} is the current under light illumination, and I_{dark} is the current in the dark. The PDCRs of the $Si/ZnGa_2O_4$ PD and $Si/SiO_2/ZnGa_2O_4$ PD each as a function of bias voltage are shown in Fig. 2(c). The PDCR of the $Si/SiO_2/ZnGa_2O_4$ PD at reverse bias was obviously higher than that of the $Si/ZnGa_2O_4$ PD. At −1 V bias, the PCDR of the $Si/SiO_2/ZnGa_2O_4$ PD was 10^5, a value $\sim 2 \times 10^3$ times higher than the PCDR value of 48 for the $Si/ZnGa_2O_4$ PD.

Fig. 3(a) and (b) present the levels of time dependence of the photocurrent of, respectively, the $Si/ZnGa_2O_4$ PD and $Si/SiO_2/ZnGa_2O_4$ PD, each under 254 nm wavelength illumination with the "ON" light intensity being increased step-wise with time from 65 to 1020 μW cm^{-2} at −1 V bias. Compared with the $Si/ZnGa_2O_4$ PD, the $Si/SiO_2/ZnGa_2O_4$ PD showed a better ON/OFF switching performance, with high reproducibility and stability. Fig. 3(c) shows plots of the photocurrents of the two devices each as a function of the 254 nm wavelength light intensity at −1 V bias. With increasing light intensity, the photocurrent of each device increased almost linearly. In general, photocurrent *versus* light intensity follows the equation[28–30]

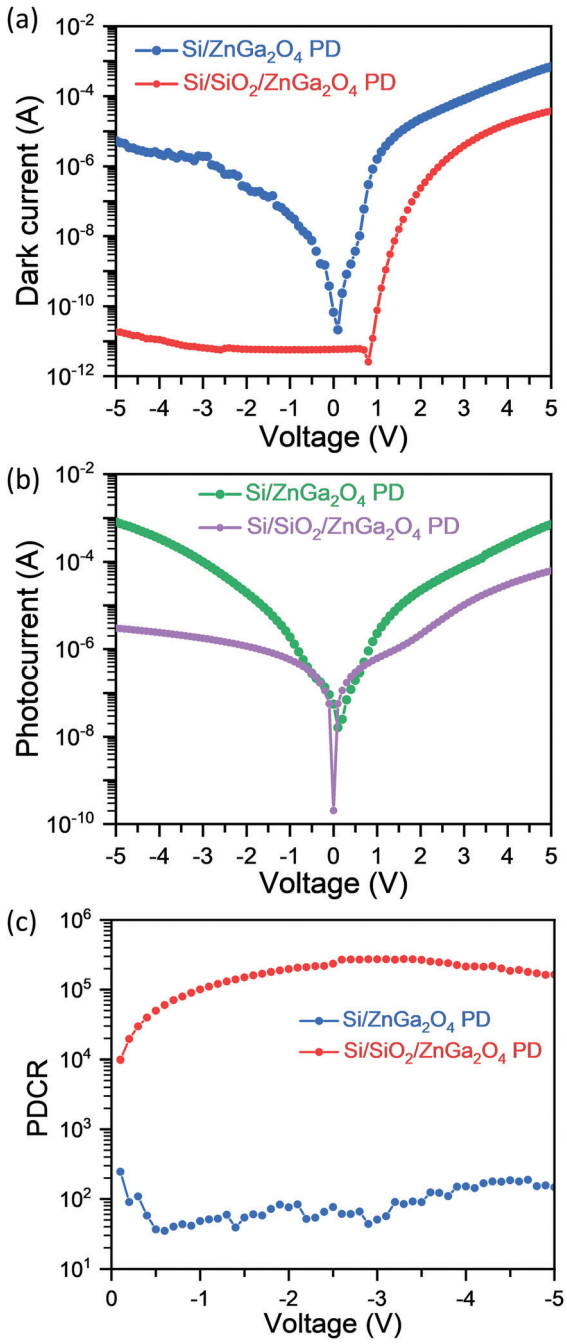

Fig. 2 (a and b) *I–V* characteristics of the $Si/ZnGa_2O_4$ PD and $Si/SiO_2/ZnGa_2O_4$ PD (a) in the dark and (b) under 254 nm wavelength UV light illumination with an intensity of 1020 μW cm^{-2}. (c) PDCRs of the $Si/ZnGa_2O_4$ PD and $Si/SiO_2/ZnGa_2O_4$ PD as a function of bias voltage.

$$I_{\mathrm{photo}} = AP^{\theta},$$

where A is a constant, P is the light intensity and θ reflects the photocurrent efficiency related to the trapping and recombination dynamics of the photo-generated carriers in the PD. By fitting this equation to the curves of photocurrent *versus* light

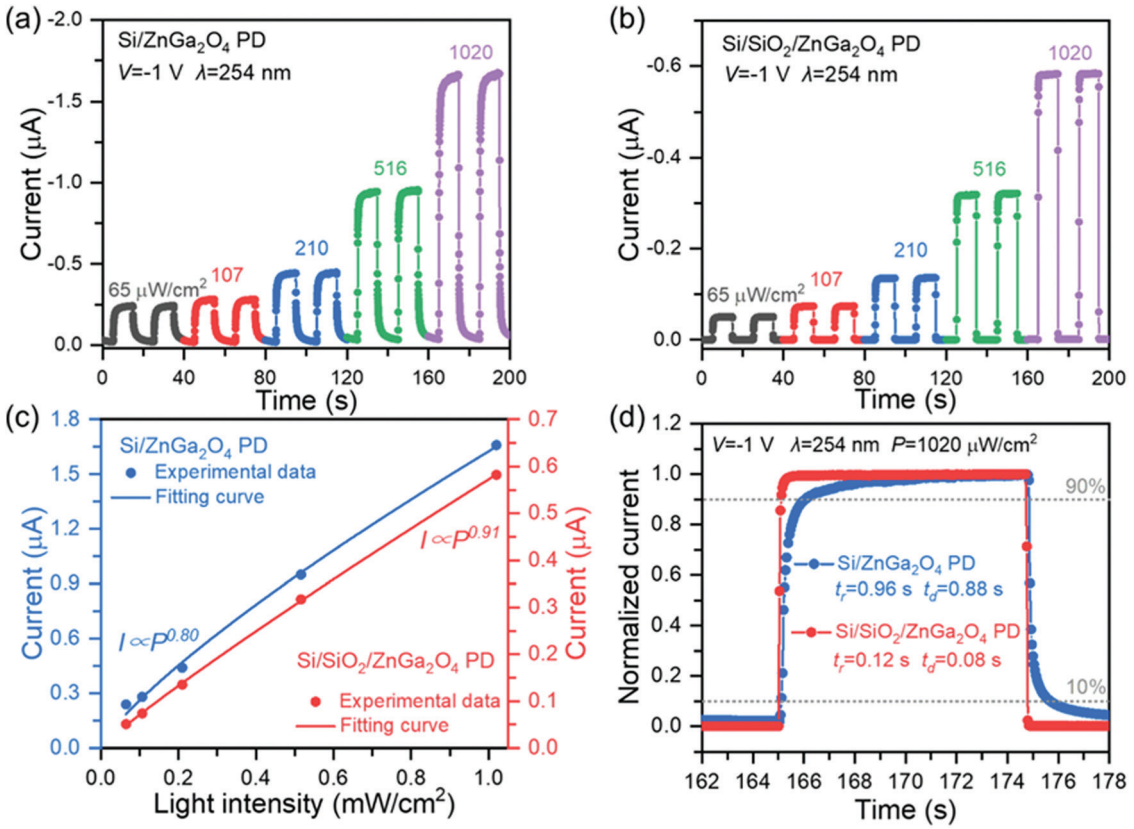

Fig. 3 (a) Time dependence of the photocurrent of the $Si/ZnGa_2O_4$ PD and (b) that of the $Si/SiO_2/ZnGa_2O_4$ PD, each under 254 nm wavelength illumination with the "ON" light intensity increasing step-wise with time from 65 to 1020 μW cm^{-2} at −1 V bias. (c) Photocurrents of the $Si/ZnGa_2O_4$ PD and $Si/SiO_2/ZnGa_2O_4$ PD each as a function of intensity of 254 nm wavelength light at −1 V bias. (d) The enlarged normalized transient current photoresponses of the $Si/ZnGa_2O_4$ PD and $Si/SiO_2/ZnGa_2O_4$ PD each under 254 nm wavelength illumination with an intensity of 1020 μW cm^{-2} at −1 V bias.

intensity of our $Si/ZnGa_2O_4$ PD and $Si/SiO_2/ZnGa_2O_4$ PD (Fig. 3(c)), θ values of, respectively, 0.80 and 0.91 were obtained. These results indicated that the insertion of the SiO_2 layer could suppress the formation of interface defect states, thereby reducing the trapping and recombination of carriers at the interface.[31]

To evaluate the response speed of the devices, the normalized transient current photoresponses of the $Si/ZnGa_2O_4$ PD and $Si/SiO_2/ZnGa_2O_4$ PD to 254 nm wavelength illumination with an intensity of 1020 μW cm^{-2} at −1 V bias were obtained, as shown in Fig. 3(d). The $Si/SiO_2/ZnGa_2O_4$ PD showed an obviously more rapid response than did the $Si/ZnGa_2O_4$ PD. Rise time and decay time (t_r and t_d) are defined as the times for the photocurrent to, respectively, increase from 10% to 90% and decrease from 90% to 10% of the maximum value. Notably, the introduction of the SiO_2 layer was found to be associated with significant decreases in t_r and t_d from 0.96 s to 0.12 s and from 0.88 s to 0.08 s, respectively. According to previous reports, the response time of a heterojunction PD is usually determined by the resistor–capacitor (RC) time constant, the time of diffusion of carriers to the junction depletion region, the transit time of carrier drift across the depletion region, and the interface trapping effect.[25,32] To determine the main reason for the response speed of our devices, various $Si/SiO_2/ZnGa_2O_4$ heterojunctions with different thicknesses of the SiO_2 layer (from 50 nm to 150 nm) were fabricated and investigated using the same process. As the thickness of the SiO_2 insulating layer was increased, the capacitance of the heterojunction gradually decreased, but the response time (t_r = 0.12 s, t_d = 0.08 s) was almost unchanged, as shown in Fig. S5 (ESI†). Therefore, the RC constant was determined to not be the main factor affecting the response speed of our devices. Additionally, the carrier diffusion speed and drift speed were expected to be similar for the devices with and without the SiO_2 layer, and thus were not considered to be the main reason for the difference in the response speed. The relationship between photocurrent and light intensity, shown in Fig. 3(c), indicated that the insertion of the SiO_2 layer could reduce the density of interface defects. Thus, the SiO_2-interfacial-layer-associated acceleration of response speed was concluded to be mainly responsible for the reduction in the extent of carrier trapping at the interface defects.[31,33,34] The time-dependent photoresponse characteristics of $Si/SiO_2/ZnGa_2O_4$ PD under 254 nm wavelength illumination with an intensity of 1020 μW cm^{-2} at different bias voltages are shown in Fig. S6 (ESI†). This PD displayed excellent stability under reverse bias, and the response speed of the

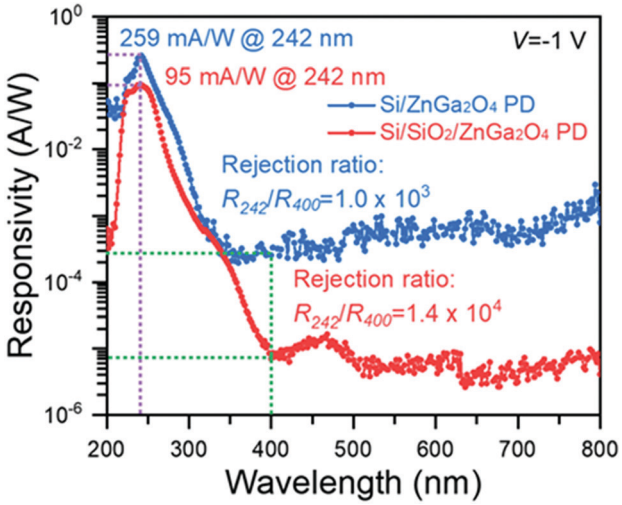

Fig. 4 Spectral responses of the $Si/ZnGa_2O_4$ PD and $Si/SiO_2/ZnGa_2O_4$ PD from 200 nm to 800 nm at −1 V bias.

device was almost unchanged as the bias was increased from −1 V to −5 V.

The responsivity of the device can be calculated by using the formula[35–37]

$$R = (I_{\text{photo}} - I_{\text{dark}})/PS$$

where P is the incident light intensity, and S is the effective area under irradiation. Fig. 4 shows the spectral responses of the $Si/ZnGa_2O_4$ PD and $Si/SiO_2/ZnGa_2O_4$ PD from 200 nm to 800 nm at −1 V bias. The peak responsivity levels of the devices with and without the SiO_2 layer at a wavelength of 242 nm were approximately 95 mA W^{-1} and 259 mA W^{-1}, respectively. The decreased peak responsivity of the $Si/SiO_2/ZnGa_2O_4$ PD may be associated with the strong blocking effect of the SiO_2 insulating layer on photogenerated carriers. The −3 dB cut-off wavelengths of $Si/ZnGa_2O_4$ PD and $Si/SiO_2/ZnGa_2O_4$ PD were both determined to be about 250 nm. Moreover, the UV-visible rejection ratio, defined as the ratio between the peak responsivity and responsivity at 400 nm, was greatly enhanced from 1.0×10^3 to 1.4×10^4 upon the introduction of the SiO_2 layer.

Detectivity is another vital parameter for evaluating the performance of a PD and can be calculated using the equation[38–40]

$$D^* = R\Big/\sqrt{2eI_{\text{dark}}/S}$$

where e is the elemental charge. With the introduction of the SiO_2 interfacial layer, the detectivity of the device at −1 V greatly increased from 2.35×10^{11} cm $Hz^{1/2}$ W^{-1} to 7.03×10^{12} cm $Hz^{1/2}$ W^{-1}, and this increase was due to the significant reduction of the dark current. Table 1 summarizes the performance parameters of typical Si-based heterojunction UV PDs. Our $Si/SiO_2/ZnGa_2O_4$ PD clearly showed the largest UV-visible rejection ratio and PDCR. Moreover, the response speed and detectivity of our $Si/SiO_2/ZnGa_2O_4$ PD were also found to be better than those of most Si-based heterojunction UV PDs.

To gain a good understanding of the influence of the SiO_2 interfacial layer on the photodetection performance of the device, Anderson-model-derived energy band diagrams of the $Si/ZnGa_2O_4$ and $Si/SiO_2/ZnGa_2O_4$ structures were drawn, as shown in Fig. 5. To draw the energy band diagram, the band gap E_g and electron affinity χ values of Si and $ZnGa_2O_4$ were taken from previous reports: E_g(Si) ∼ 1.12 eV, E_g ($ZnGa_2O_4$) ∼ 5.2 eV; χ(Si) ∼ 4.05 eV, χ($ZnGa_2O_4$) ∼ 2.31 eV.[26,48] A type-I band alignment was obtained in the $Si/ZnGa_2O_4$ heterojunction with the valence-band and conduction-band offsets of 1.74 eV and 2.34 eV, respectively. In addition, based on SiO_2 electron affinity and band gap values of ∼0.9 eV and ∼9.0 eV, respectively,[26] the conduction band offset of Si/SiO_2 was determined to be ∼3.15 eV, and the valence band offset of $SiO_2/ZnGa_2O_4$ was determined to be ∼2.39 eV. For the $Si/ZnGa_2O_4$ PD, solar-blind UV light and visible light are mainly absorbed by the $ZnGa_2O_4$ layer and Si substrate, respectively.[3] Clearly, the introduction of the SiO_2 layer could yield a sufficient blocking of the transport of electrons generated in Si under visible-light illumination to the $ZnGa_2O_4$ layer. Therefore, the $Si/SiO_2/ZnGa_2O_4$ PD showed an obvious suppression of visible-light photoresponse and thus a high UV-visible rejection ratio. Meanwhile, under the solar-blind UV light illumination, the large valence band offset of $SiO_2/ZnGa_2O_4$ prevented the photogenerated holes in the $ZnGa_2O_4$ layer from crossing into the Si; hence the responsivity of the $Si/SiO_2/ZnGa_2O_4$ PD was lower than that of the $Si/ZnGa_2O_4$ PD.

Table 1 The reported performance parameters of typical Si-based heterojunction UV PDs

Devices	Dark current	Photo-to-dark current ratio	Rise/decay time	Peak responsivity (R_p, mA W^{-1})	UV-visible rejection ratio	Detectivity (cm $Hz^{1/2}$ W^{-1})	Ref.
p-MgZnO : Sb/n-Si	0.96 μA @ −5 V	—	<100 ms	320 @ −30 V	—	3.65×10^{11}	41
p-Si/n-ZnO	7.19 μA @ −2 V	—	0.44 s/0.59 s	21 510 @ −2 V	—	1.26×10^{12}	42
p-Si/n-ZnO	∼1 μA @ −2 V	—	—	340 @ −2 V	—	2.11×10^{12}	43
p-Si/n-$ZnGa_2O_4$	0.027 nA @ 2 V	490	0.25 s/0.067 s	—	—	—	13
p-NiO/n-Si	—	—	1.53 s/0.7 s	160 @ −5 V	—	—	44
p-Si/n-Ga_2O_3	0.85 μA @ 3 V	940	1.79 s/0.27 s	370 000 @ 3 V	—	—	45
p-Si/i-MgO/n-ZnO	∼2 μA @ −5 V	4.5×10^4	47 s/—	—	334.3 (R_p/R_{500})	1.15×10^{13}	46
p-NiO/i-NiO/n-Si	0.54 μA @ −2 V	—	—	—	915.3 (R_p/R_{500})	—	47
p-Si/i-MgO/n-ZnO	0.5 nA @ −2 V	—	—	—	45 (R_p/R_{400})	—	18
p-Si/n-$ZnGa_2O_4$	38 nA @ −1 V	48	0.96 s/0.88 s	259 @ −1 V	1.0×10^3(R_p/R_{400})	2.35×10^{11}	This work
p-Si/i-SiO_2/n-$ZnGa_2O_4$	5.7 pA @ −1 V	10^5	0.12 s/0.08 s	95 @ −1 V	1.4×10^4(R_p/R_{400})	7.03×10^{12}	This work

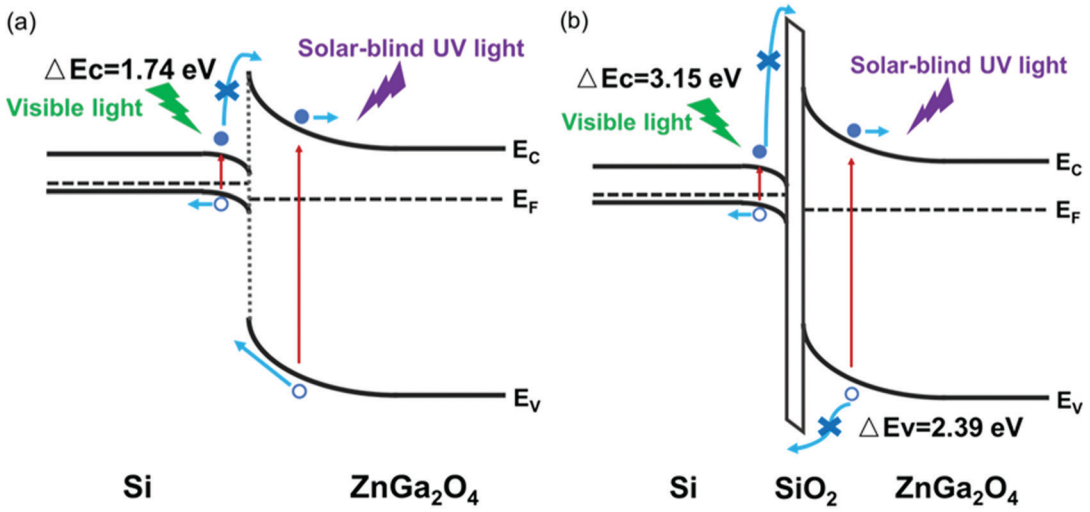

Fig. 5 Energy band diagrams of the (a) Si/$ZnGa_2O_4$ heterojunction and (b) Si/SiO_2/$ZnGa_2O_4$ heterojunction under solar-blind UV light and visible light at reverse bias.

Conclusions

In summary, we demonstrated a performance enhancement of a p-Si/n-$ZnGa_2O_4$ heterojunction solar-blind UV PD by inserting a SiO_2 interfacial layer. Compared with the dark current at −1 V bias of the Si/$ZnGa_2O_4$ PD, that of the Si/SiO_2/$ZnGa_2O_4$ PD was more than three orders of magnitude lower. With the introduction of the SiO_2 interfacial layer, the photo-to-dark current ratio and the detectivity of the device were greatly improved due to the substantial reduction of dark current. The insertion of the SiO_2 layer reduced the carrier trapping at the interface defects, resulting in a significant increase in the response speed of the device. Moreover, the large conduction band offset of Si/SiO_2 could effectively block visible-light-generated electrons in Si, thereby suppressing the visible-light response and enhancing the UV-visible rejection ratio of the Si/SiO_2/$ZnGa_2O_4$ PD. Our work has provided a feasible method for constructing high-performance Si-based heterojunction solar-blind UV PDs.

Author contributions

All of the authors contributed to the writing of the manuscript, and have given approval to the final version of the manuscript.

Conflicts of interest

There are no conflicts to declare.

Acknowledgements

This work is supported by the National Natural Science Foundation of China (62074148, 61875194, 11727902, 12074372, 11774341, 11974344, 61975204, 11804335), 100 Talents Program of the Chinese Academy of Sciences, Youth Innovation Promotion Association, CAS (2020225), and Open Project of the State Key Laboratory of Luminescence and Applications (SKLA-2020-02, SKLA-2020-06).

Notes and references

1 R. H. Huang, C. Y. Huang, S. L. Ou, T. K. Juang and P. L. Liu, *Cryst. Growth Des.*, 2017, **17**, 6071.
2 Z. Galazka, S. Ganschow, R. Schewski, K. Irmscher, D. Klimm, A. Kwasniewski, M. Pietsch, A. Fiedler, I. Schulze-Jonack, M. Albrecht, T. Schroder and M. Bickermann, *APL Mater.*, 2019, **7**, 011301.
3 D. Y. Han, K. W. Liu, Q. C. Hou, X. Chen, J. L. Yang, B. H. Li, Z. Z. Zhang, L. Liu and D. Z. Shen, *Sens. Actuators, A*, 2020, **315**, 112354.
4 S. H. Tsai, S. Basu, C. Y. Huang, L. C. Hsu, Y. G. Lin and R. H. Horng, *Sci. Rep.*, 2018, **8**, 14056.
5 R. Zhuo, L. Zeng, H. Yuan, D. Wu, Y. Wang, Z. Shi, T. Xu, Y. Tian, X. Li and Y. H. Tsang, *Nano Res.*, 2018, **12**, 183.
6 R. Zhuo, Y. Wang, D. Wu, Z. Lou, Z. Shi, T. Xu, J. Xu, Y. Tian and X. Li, *J. Mater. Chem. C*, 2018, **6**, 299.
7 J. X. Chen, W. X. Ouyang, W. Yang, J. H. He and X. S. Fang, *Adv. Funct. Mater.*, 2020, **30**, 1909909.
8 T. R. Paudel, A. Zakutayev, S. Lany, M. d'Avezac and A. Zunger, *Adv. Funct. Mater.*, 2011, **21**, 4493.
9 A. De Vos, K. Lejaeghere, D. E. Vanpoucke, J. J. Joos, P. F. Smet and K. Hemelsoet, *Inorg. Chem.*, 2016, **55**, 2402.
10 Y. Jang, S. Hong, J. Seo, H. Cho, K. Char and Z. Galazka, *Appl. Phys. Lett.*, 2020, **116**, 202104.
11 E. Chikoidze, C. Sartel, I. Madaci, H. Mohamed, C. Vilar, B. Ballesteros, F. Belarre, E. del Corro, P. Vales-Castro, G. Sauthier, L. Li, M. Jennings, V. Sallet, Y. Dumont and A. Pérez-Tomás, *Cryst. Growth Des.*, 2020, **20**, 2535.
12 Y. Shi, P. F. Ndione, L. Y. Lim, D. Sokaras, T. C. Weng, A. R. Nagaraja, A. G. Karydas, J. D. Perkins, T. O. Mason and D. S. Ginley, *Chem. Mater.*, 2014, **26**, 1867.

13 W. Lin, D. Zhang, S. Liu, Y. Li, W. Zheng and F. Huang, *Mater. Lett.*, 2021, **283**, 128805.
14 S. S. Yi, J. S. Bae, B. K. Moon, J. H. Jeong, I. W. Kim and H. L. Park, *Appl. Phys. A: Mater. Sci. Process.*, 2003, **76**, 433.
15 Y. Huang, F. Zhuge, J. Hou, L. Lv, P. Luo, N. Zhou, L. Gan and T. Zhai, *ACS Nano*, 2018, **12**, 4062.
16 U. Otuonye, H. W. Kim and W. D. Lu, *Appl. Phys. Lett.*, 2017, 110.
17 K. B. Ko, B. D. Ryu, M. Han, C.-H. Hong, T. A. Doan and T. V. Cuong, *J. Alloys Compd.*, 2020, **823**, 153884.
18 T. C. Zhang, Y. Guo, Z. X. Mei, C. Z. Gu and X. L. Du, *Appl. Phys. Lett.*, 2009, **94**, 113508.
19 J.-D. Hwang, D.-H. Wu and S.-B. Hwang, *IEEE Photonics Technol. Lett.*, 2014, **26**, 1081.
20 M. Ding, Z. Guo, X. Chen, X. Ma and L. Zhou, *Nanomaterials*, 2020, **10**, 362.
21 Z. Liang, P. Zeng, P. Liu, C. Zhao, W. Xie and W. Mai, *ACS Appl. Mater. Interfaces*, 2016, **8**, 19158.
22 S. Demchyshyn, M. Verdi, L. Basirico, A. Ciavatti, B. Hailegnaw, D. Cavalcoli, M. C. Scharber, N. S. Sariciftci, M. Kaltenbrunner and B. Fraboni, *Adv. Sci.*, 2020, **7**, 2002586.
23 H. Zhou, P. Gui, Q. Yu, J. Mei, H. Wang and G. Fang, *J. Mater. Chem. C*, 2015, **3**, 990.
24 G. Cen, Y. Liu, C. Zhao, G. Wang, Y. Fu, G. Yan, Y. Yuan, C. Su, Z. Zhao and W. Mai, *Small*, 2019, **15**, 1902135.
25 G. Yan, C. Zeng, Y. Yuan, G. Wang, G. Cen, L. Zeng, L. Zhang, Y. Fu, C. Zhao, R. Hong and W. Mai, *ACS Appl. Mater. Interfaces*, 2019, **11**, 32097.
26 Y.-R. Li, C.-Y. Wan, C.-T. Chang, Y.-C. Huang, W.-L. Tsai, I. C. Lee and H.-C. Cheng, *IEEE Electron Device Lett.*, 2015, **36**, 850.
27 D.-Y. Jiang, X.-Y. Zhang, Q.-S. Liu, Z.-H. Bai, L.-P. Lu, X.-C. Wang, X.-Y. Mi, N.-L. Wang and D.-Z. Shen, *Appl. Surf. Sci.*, 2010, **256**, 6153.
28 Z. Zhao, D. Wu, J. Guo, E. Wu, C. Jia, Z. Shi, Y. Tian, X. Li and Y. Tian, *J. Mater. Chem. C*, 2019, **7**, 12121.
29 X. Zhou, Q. Zhang, L. Gan, X. Li, H. Li, Y. Zhang, D. Golberg and T. Zhai, *Adv. Funct. Mater.*, 2016, **26**, 704.
30 L. Zeng, D. Wu, J. Jie, X. Ren, X. Hu, S. P. Lau, Y. Chai and Y. H. Tsang, *Adv. Mater.*, 2020, **32**, 2004412.
31 C. Wei, J. Xu, S. Shi, R. Cao, J. Chen, H. Dong, X. Zhang, S. Yin and L. Li, *J. Mater. Chem. C*, 2019, **7**, 9369.
32 E. Monroy, E. Muñoz, F. J. Sánchez, F. Calle, E. Calleja, B. Beaumont, P. Gibart, J. A. Muñoz and F. Cussó, *Semicond. Sci. Technol.*, 1998, **13**, 1042.
33 X. Li, M. Zhu, M. Du, Z. Lv, L. Zhang, Y. Li, Y. Yang, T. Yang, X. Li, K. Wang, H. Zhu and Y. Fang, *Small*, 2016, **12**, 595–601.
34 Z. P. Wu, L. Jiao, X. L. Wang, D. Y. Guo, W. H. Li, L. H. Li, F. Huang and W. H. Tang, *J. Mater. Chem. C*, 2017, **5**, 8688.
35 D. Wu, Z. Zhao, W. Lu, L. Rogée, L. Zeng, P. Lin, Z. Shi, Y. Tian, X. Li and Y. H. Tsang, *Nano Res.*, 2021, **14**, 1973.
36 Y. Ji, W. Xu, N. Ding, H. Yang, H. Song, Q. Liu, H. Agren, J. Widengren and H. Liu, *Light: Sci. Appl.*, 2020, **9**, 184.
37 Z. Lu, Y. Xu, Y. Yu, K. Xu, J. Mao, G. Xu, Y. Ma, D. Wu and J. Jie, *Adv. Funct. Mater.*, 2020, **30**, 1907951.
38 R. R. Zhuo, D. Wu, Y. G. Wang, E. P. Wu, C. Jia, Z. F. Shi, T. T. Xu, Y. T. Tian and X. J. Li, *J. Mater. Chem. C*, 2018, **6**, 10982.
39 B. Qiao, Z. Zhang, X. Xie, B. Li, K. Li, X. Chen, H. Zhao, K. Liu, L. Liu and D. Shen, *J. Phys. Chem. C*, 2019, **123**, 18516.
40 D. Wu, C. Jia, F. Shi, L. Zeng, P. Lin, L. Dong, Z. Shi, Y. Tian, X. Li and J. Jie, *J. Mater. Chem. A*, 2020, **8**, 3632.
41 R. Bhardwaj, P. Sharma, R. Singh and S. Mukherjee, *IEEE Photonics Technol. Lett.*, 2017, **29**, 1215.
42 T. H. Flemban, M. A. Haque, I. Ajia, N. Alwadai, S. Mitra, T. Wu and I. S. Roqan, *ACS Appl. Mater. Interfaces*, 2017, **9**, 37120.
43 S. K. Singh, P. Hazra, S. Tripathi and P. Chakrabarti, *Superlattices Microstruct.*, 2016, **91**, 62.
44 N. H. Al-Hardan, N. M. Ahmed, M. A. Almessiere and A. A. Aziz, *Mater. Res. Express*, 2020, **6**, 126332.
45 X. C. Guo, N. H. Hao, D. Y. Guo, Z. P. Wu, Y. H. An, X. L. Chu, L. H. Li, P. G. Li, M. Lei and W. H. Tang, *J. Alloys Compd.*, 2016, **660**, 136.
46 J.-D. Hwang and C.-Y. Liao, *J. Phys. Chem. C*, 2020, **124**, 12734.
47 J. D. Hwang and Y. T. Hwang, *Nanotechnology*, 2020, **31**, 345205.
48 Y.-C. Shen, C.-Y. Tung, C.-Y. Huang, Y.-C. Lin, Y.-G. Lin and R.-H. Horng, *ACS Appl. Electron. Mater.*, 2019, **1**, 783.